The Astrophysical Journal, 872:110 (7pp), 2019 February 10 https://doi.org/10.3847/1538-4357/aafda7

On the Common Origin of Cosmic Rays across the Ankle and Diffuse Neutrinos at the Highest Energies from Low-luminosity Gamma-Ray Bursts

Denise Boncioli, Daniel Biehl, and Walter Winter
Deutsches Elektronen-Synchrotron (DESY), Platanenallee 6, D-15738 Zeuthen, Germany; denise.boncioli@desy.de
Received 2018 September 19; revised 2019 January 9; accepted 2019 January 9; published 2019 February 14

Abstract

We demonstrate that the ultra-high-energy cosmic rays (UHECRs) produced in the nuclear cascade in the jets of low-luminosity gamma-ray bursts (LL-GRBs) can describe the UHECR spectrum and composition, and at the same time, the diffuse neutrino flux at the highest energies. The radiation density in the source simultaneously controls the neutrino production and the development of the nuclear cascade, leading to a flux of nucleons and light nuclei describing even the cosmic-ray ankle at $5 \cdot 10^{18}$ eV. The derived source parameters are consistent with population studies, indicating a baryonic loading factor of about 10. Our results motivate the continued experimental search of LL-GRBs as a unique GRB population.

Key words: cosmic rays – gamma-ray burst: general – neutrinos

1. Introduction

Gamma-ray bursts (GRBs) are extreme electromagnetic outbursts; see, for example, Piran (2004). Here, we consider the possibility that low-luminosity GRBs (LL-GRBs, with isotropic luminosity $\lesssim 10^{49}\,\mathrm{erg\,s^{-1}}$) and high-luminosity GRBs (HL-GRBs, with isotropic luminosity $\gtrsim 10^{49}\,\mathrm{erg\,s^{-1}}$) are two distinct populations, based on the different local rates of the two samples (Guetta & Della Valle 2007; Liang et al. 2007; Virgili et al. 2009; Sun et al. 2015). Because they are locally much more abundant than HL-GRBs ($\approx 1\,\mathrm{Gpc^{-3}\,yr^{-1}}$), LL-GRBs ($\approx 300\,\mathrm{Gpc^{-3}\,yr^{-1}}$, as predicted in Liang et al. 2007) have been proposed as sources of cosmic rays and neutrinos (Murase et al. 2006, 2008; Liu et al. 2011; Senno et al. 2016). More recently, LL-GRBs as sources of ultra-high-energy cosmic-ray (UHECR) nuclei have been studied in Zhang et al. (2018), including possible injection compositions. Due to the low radiation density, it has been proposed that the nuclei can escape intact from the sources, leading to compatibility with the UHE chemical composition measured by the Pierre Auger Observatory (Aab et al. 2014) after propagation. However, the low radiation density required for nuclei to escape implies at the same time that there are low neutrino production efficiencies—possibly too low to simultaneously describe the diffuse neutrino flux in a one-zone model.

HL-GRBs have been tested as the possible origin of UHECRs for both protons in Baerwald et al. (2015) and nuclei in Biehl et al. (2018a) describing cosmic-ray and neutrino data explicitly. It has been shown that for nuclei and for high enough radiation densities, a nuclear cascade due to the photodisintegration of nuclei develops—while at the same time neutrinos are efficiently produced by photohadronic interactions. Very tight constraints on neutrinos from HL-GRBs have been obtained using direction, timing, and energy information from GRB catalogs for stacking limits (Abbasi et al. 2012; Aartsen et al. 2017). These constraints limit the parameter space to low radiation densities, such as high-collision radii and low luminosities in the internal shock model—parameters that may not be favorable for HL-GRBs, and point already toward LL-GRBs (Biehl et al. 2018a). A possible caveat are multi-zone collision models in which the different messengers originate from different regions of the same GRB, predicting somewhat lower neutrino fluxes (Bustamante et al. 2015, 2017; Globus et al. 2015a)—which, however, cannot explain the diffuse neutrino flux. The stacking bounds do not apply to LL-GRBs due to their much longer duration (making the background suppression less efficient) and their low luminosity (limiting the detection of resolved sources). Note that the luminosity mentioned here represents the X-ray luminosity, which may differ from the intrinsic kinetic luminosity of the jet. The latter can be higher by a factor ∼100, taking into account the energy conversion efficiency (Aloy et al. 2018).

In this work, we study if LL-GRBs with a nuclear cascade in the jet can power the diffuse neutrino and cosmic-ray fluxes at the highest energies at the same time, using methods similar to those of Biehl et al. (2018a, 2018b). We inject a nuclear composition that is found to be reasonable in the jets of GRB progenitors (Woosley & Heger 2006; Zhang et al. 2018), and we include the transition to the next population (at lower energies). As an important ingredient, it was noted in Unger et al. (2015) in a generic model and in Globus et al. (2015b) and Biehl et al. (2018a) that for GRBs the nuclear cascade also controls the production of nucleons below the change of the slope in the measured CR energy spectrum, called the "ankle" at $\sim 5 \cdot 10^{18}$ eV (Fenu et al. 2017), i.e., the spectrum and composition may be described in a much larger energy range across the ankle. Our analysis is based on a combined source-propagation model, which means that we include the interactions of the injected nuclei in the source in addition to the UHECR propagation, whereas a propagation-only model starts off at the interface between source and extragalactic space. Compared to earlier studies, we perform extensive parameter space scans, focusing on a combined description of UHECR and neutrino data and including the description of the cosmic-ray ankle. Similar to previous studies, we use the internal shock scenario as a baseline scenario and comment on alternatives where applicable. We also encourage future searches in next-generation telescopes such as CTA.

2. Methods

Motivated by diffusive shock acceleration in the jet, we assume that the spectrum of the primary injected nuclei follows a power law $\propto E^{-2}\exp(-E/E_{\rm max})$. The maximal energy $E_{\rm max}$ is determined from the balance between acceleration and interaction rates, where we take into account adiabatic cooling, photohadronic interactions, and synchrotron losses. The acceleration rate is given by $t'^{-1}_{\rm acc} = \eta c/R'_L$, with the acceleration efficiency η and the Larmor radius $R'_L = E'/ZeB'$ of a particle with energy E' and charge number Z (primed quantities refer to the shock rest frame); we use efficient acceleration $\eta \simeq 1$ in this study, which is degenerate with the injected composition and the energy scale uncertainties of Auger, as discussed in Biehl et al. (2018b). Our injection composition is a simplified version of the silicon-rich case defined in Zhang et al. (2018; 60% ^{16}O and 40% ^{28}Si into the jet).

The target photon field of the GRB prompt emission is modeled as a broken power law with lower and upper spectral indices $\beta_1 = 1.0$ and $\beta_2 = 2.0$, respectively, and a break energy that is typically around $\varepsilon'_{\gamma,\rm br} \sim 1$ keV. We have tested that our results are not very sensitive to the exact values presented here. Accelerated nuclei interact with these target photons in internal shocks at a distance $R \simeq 2\Gamma^2 ct_v$ from the engine, where Γ represents the Lorentz factor and t_v is the variability timescale of the emission. In our calculations, we fix $\Gamma \simeq 10$ (Aloy et al. 2018) and vary the radius R over a large range between 10^8 and 10^{12} km. The time variability thus changes from 10^0 to 10^4 s. We assume a total duration of $\sim 2\cdot 10^5$ s, which may be somewhat longer than the typical durations expected from observations (10^3–10^4 s). However, for GRBs with shorter durations (of the order of tens of seconds), the jet breakout time might be too large for the jet to be successfully launched (Bromberg et al. 2011). Such choked jet sources are generally not expected to emit UHECRs, as cosmic rays strongly cool in the environment, possibly producing high-energy neutrinos (He et al. 2018). Furthermore, note that our results will be degenerate in the duration times baryonic loading times apparent local rate, which means shorter durations can, e.g., be compensated for by larger baryonic loadings. Changes in the Lorentz factor can be compensated for by adjusting the radius or the variability timescale. The parameters chosen here are consistent with the ones used for jet formation and survival (Aloy et al. 2018).

To simulate the nuclear interactions within the LL-GRB jet, following Biehl et al. (2018a, 2018b), we use the *NeuCosmA* code, which is based on SOPHIA (Mucke et al. 2000) for photomeson production (photon energy in nucleus' rest frame $\varepsilon_\gamma \gtrsim 150$ MeV). For photomeson production of nuclei, a superposition model is used accordingly, i.e., the cross sections scale approximately with the nucleus' mass number $\sigma_{A\gamma} \approx A\sigma_{p\gamma}$. The photodisintegration ($\varepsilon_\gamma \lesssim 150$ MeV) cross sections are taken from CRPropa 2 ($A < 12$) (Kampert et al. 2013) and TALYS ($A \geqslant 12$) (Koning et al. 2007). For details on the interaction models, see Boncioli et al. (2017).

A critical ingredient connecting the physics of the source and the propagation of UHECRs is the cosmic-ray escape mechanism from the source. One possibility for GRBs was proposed in Baerwald et al. (2013), who postulated that even in an expanding shell, the particles within the Larmor radius of the edge of the shell can escape. As a consequence, the escape rate scales $\propto R'_L \propto E'$, which means that the escaping spectra are one power harder than the spectra within the source ("direct escape"). A similar result is obtained for Bohm-like diffusion of particles escaping a compact region. If it is assumed that only the particles at the highest energies can escape, the spectrum may be even harder, as in Globus et al. (2015a) or in Zhang et al. (2018), where the ejected spectra are defined as $\propto\exp(-\ln^2(E/E_{\rm max}))$, as found in Ohira et al. (2010); we refer to this case as "hard escape." We use this choice in this study, because we have verified that this assumption is favored by the UHECR data with respect to the direct escape for the source evolution used for LL-GRBs.

Due to their low luminosities, LL-GRBs can be only observed in the local universe. On the other hand, LL-GRBs can have much longer durations than their high-luminosity counterparts, which is likely related to the core-collapse supernovae progenitor scenario; they are thus assumed to exist up to high redshifts. For this reason, the propagation of the UHECRs ejected by a population of (in the cosmologically comoving frame) identical LL-GRBs is simulated up to $z = 6$, including the production of cosmogenic neutrinos. This is computed with the *SimProp* code (Aloisio et al. 2017), using the extragalactic background light from Gilmore et al. (2012) and the TALYS photodisintegration model from Koning et al. (2007), whose implementation is explained in Alves Batista et al. (2015). We parameterize the evolution of the LL-GRBs with redshift relative to the star formation rate (SFR) given in Hopkins & Beacom (2006) as $(1+z)^m \times H_{\rm SFR}(z)$; we consider $0 \leqslant m \leqslant 1$ in this work.

We perform a fit of the UHECR spectrum (Valiño et al. 2015) and composition (Porcelli et al. 2015), as measured by the Pierre Auger Collaboration, in two steps. First, we fit the UHECR spectrum and composition above 10^{19} eV (super-ankle component). Second, in order to describe the transition to the next (sub-ankle, which can be of Galactic origin) component at lower energies, we model the end of that population as an additional power-law spectrum. We then re-fit the relative weights of the sub- and super-ankle components, considering the energy range above 10^{18} eV.

In total, our source-propagation model has the following parameters: the collision radius R [km] (degenerate with the Lorentz factor Γ), the X-ray luminosity $L_{\rm X}$ [erg s^{-1}], the emissivity of the extragalactic component $\mathcal{L}_{\rm ej}$ [erg Mpc^{-3} yr^{-1}], the normalization of the sub-ankle component $f_{\rm Gal}$ (in terms of percentage of the total flux, and we define it at a fixed energy corresponding to $\log_{10}(E/{\rm eV}) = 17.5$), and the spectral index of the sub-ankle component α. The quality of the fit is evaluated by computing the χ^2 of the unfolded spectrum and composition data points. The latter ones are treated using the $\ln A$ parameterization given in Pierre Auger Collaboration (2013). The quantity $\mathcal{L}_{\rm ej}$ is referred to the total CR spectrum ejected by the source. Since we use a source-propagation model in this study, it is possible to compute this quantity and compare it to the injection spectrum $\mathcal{L}_{\rm inj} \propto \int E\cdot E^{-2}\exp(-E/E_{\rm max})dE$. The baryonic loading $\xi_{\rm A}$, i.e., the ratio between energy injected as CR nuclei and the total X-ray energy $E_{\rm X}$, can be then obtained as $\xi_{\rm A} = \mathcal{L}_{\rm inj}/(\dot{n}_{\rm LL-GRB}(z=0)\cdot E_{\rm X})$. In this work, we adopt $\dot{n}_{\rm LL-GRB}(z=0) = 300$ Gpc^{-3} yr^{-1}, in agreement with the results of Liang et al. (2007), where $\dot{n}_{\rm LL-GRB}(z=0) = 325^{+352}_{-177}$ Gpc^{-3} yr^{-1} is found. Changes of the value of the local rate of the LL-GRBs and of the total duration of the burst are degenerate with the baryonic loading.

We show in Figure 1 a comparison between the propagation-only model (dashed curves), corresponding to Zhang et al.

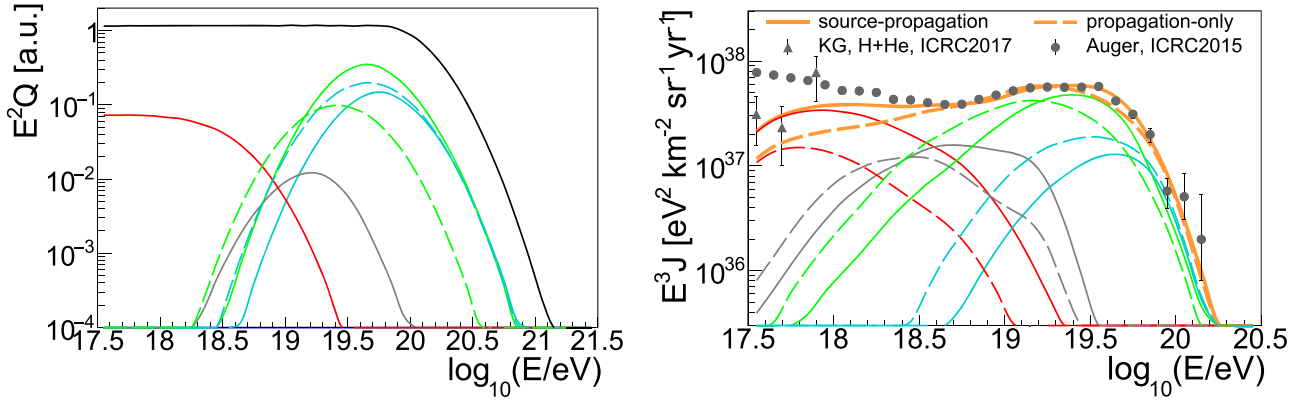

Figure 1. Comparison between the propagation-only model (dashed curves), corresponding to Zhang et al. (2018), and the source-propagation model (solid curves), including the nuclear disintegration in the source corresponding to Biehl et al. (2018a), for the same injection composition and parameters. Left: cosmic-ray fluxes escaping from the source (multiplied by E^2). The dashed curves refer to the spectra coming out of the source given by Equation (7) in Zhang et al. (2018; green $A = 16$ and cyan $A = 28$). The solid curves refer to a power-law acceleration spectrum $\propto E^{-2}\exp(-E/E_{\rm max})$ (black curve, sum of 60% $A = 16$ and 40% $A = 28$) injected within the source and to the groups of isotopes generated by the interactions in the source (red $A = 1$, gray $2 \leqslant A \leqslant 4$, green $5 \leqslant A \leqslant 24$, cyan $25 \leqslant A \leqslant 28$). Right: cosmic-ray fluxes at detection (multiplied by E^3). For comparison, the Auger data points from Valiño et al. (2015) and the KASCADE-Grande data points (for the light component, H and He) from Schoo et al. (2017) are shown. The isotope groups are defined as reported above. The plots are obtained using the parameters corresponding to the best-fit as reported in Figure 3, and are independently normalized to the UHECR flux.

(2018), and the source-propagation model (solid curves), including the nuclear disintegration in the source corresponding to Biehl et al. (2018a), for the same injection composition and parameters. In the propagation-only model, the interactions in the source are not taken into account, and the ejected CR spectra into the extragalactic space are defined by ad hoc functions; they directly represent the injection composition. We also show for comparison the CR spectra (solid curves) obtained using a $\propto E^{-2}\exp(-E/E_{\rm max})$ spectrum at injection (shown as black curve), including the disintegration in the source, and applying the hard escape mechanism. In the case of the source-propagation model, only one representative isotope for each isotope group is propagated. In order to compare the models, we first normalize the propagated CR fluxes to the measured spectrum and then derive the normalization of the spectra at the source. The most relevant difference is an escaping flux of nucleons, which are generated during the development of the nuclear cascade within the source. By comparing the models after propagation (Figure 1, right panel), a clear deficit of the light component at the lowest energies is visible in the propagation-only model, compared to the source-propagation model, which could eventually require a stronger source evolution in the propagation-only case in order to describe the data. Note that that the light component of the escaping flux has a softer spectrum compared to the other ones, because neutrons are not magnetically confined (Baerwald et al. 2013). This factor turns out also to be fundamental in order to describe the CR data in the whole energy range, as already noticed in Aloisio et al. (2014), Globus et al. (2015b), and Unger et al. (2015). In addition, in a propagation-only model, the neutrino production in the source cannot be computed directly.

3. Results and Discussion

Depending on the radiation density in the source, photonuclear interactions can trigger the subsequent disruption of higher-mass nuclei into lower-mass fragments. As a consequence, the so-called nuclear cascade can develop, leading to the population of many different isotope species in the source. We show in Figure 2 (left panel) different regimes in the parameter space for the nuclear cascade (shaded regions) as a function of X-ray luminosity $L_{\rm X}$ and collision radius R for the heaviest injected mass, $A = 28$. If the photon density in the source is not high enough to cause efficient disintegration, only a few species with masses close to the injected composition are populated (empty cascade). With increasing energy density, nuclei interact more efficiently with these photons such that the source becomes optically thick to photohadronic interactions of heavy nuclei and the nuclear cascade efficiently feeds energy into lower-mass nuclei (populated cascade). For extremely high radiation densities the source becomes opaque to photohadronic interactions of nucleons (optically thick case) such that most of the baryonic energy is stored in protons and neutrons. We also show the point Z, corresponding to $R = 10^{10}$ km and $L_{\rm X} = 10^{47}$ erg s^{-1}, as the representative point in the parameter space used in Zhang et al. (2018). In the right panel of Figure 2 we show the result of the fit of the cosmic-ray spectrum and composition. The region of the parameter space, where the cosmic-ray data are best reproduced, clearly follows the contour of the maximum energy $E_{\rm max} \approx 10^{9.7}$ GeV in the source, depicted in the right panel of Figure 2. In the left panel of Figure 2 we superimpose the region where the source neutrino flux is within 1σ from the IceCube PeV data points (Kopper 2017). This region clearly shows that in order to account for the IceCube flux, a moderate level of disintegration in the source is implied. We checked that all the points of our parameter space are consistent with radiation constraints, i.e., efficient cosmic-ray acceleration is possible (Murase & Ioka 2013).

The cosmic-ray and neutrino observables corresponding to the parameter space point describing both data sets are shown in Figure 3. With the same parameters describing the CR data, the neutrino flux is found to be within the expectation for the through going muons at IceCube (Kopper 2017). Note that the shape of the neutrino spectrum does not perfectly describe the neutrino data points, which may be an effect of the limited statistics in neutrinos, or additional contributions to the neutrino flux, such as a Galactic component (Palladino & Winter 2018).

The required emissivity to fit the UHECR data is $\mathcal{L}_{\rm ej} = 5.3 \times 10^{45}$ erg Mpc^{-3} yr^{-1}, which corresponds to the

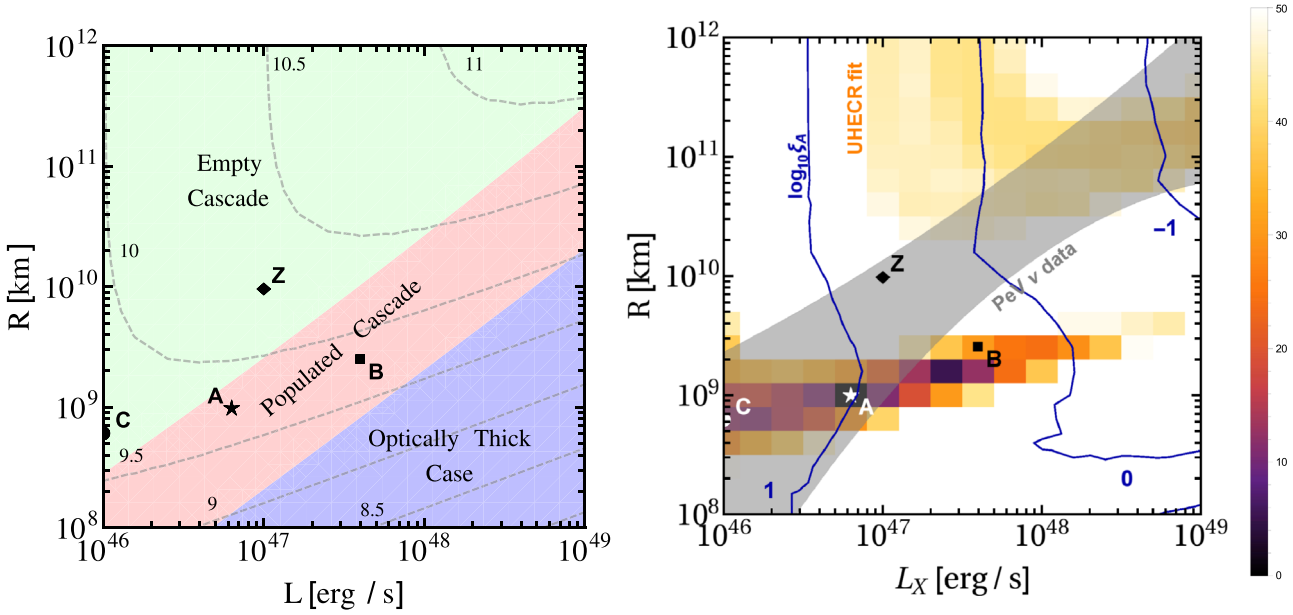

Figure 2. Parameter space study as a function of X-ray luminosity L_X and collision radius R. Left panel: different regimes in the parameter space for the nuclear cascade to develop in the source (shaded regions), as discussed in the main text. The curves show $\log_{10}(E_{\rm max}/{\rm GeV})$, with $E_{\rm max}$ being the obtained maximal energy for the injected isotope $A = 28$ in the shock rest frame. Right panel: results of the fit to UHECR data (colored contours) and PeV neutrino data (gray-shaded band) as a function of L_X and R (color scale: $(\chi^2 - \chi^2_{\rm min})$ of the fit; gray-shaded band: neutrino PeV data including uncertainties). The blue curves show isocontours of $\log_{10}\xi_A$ obtained from the cosmic-ray fit (and corresponding to the rate, $\dot{n}_{\rm LL-GRB}(z=0) = 300\ {\rm Gpc^{-3}\ yr^{-1}}$, and to the duration, $2 \cdot 10^5$ s, adopted in this study; the result is degenerate in the product of these three parameters). For each point (L_X, R), the values of the other parameters that minimize the χ^2 are used. In both panels, the stars indicate the parameters describing both UHECR and neutrino data (point A) and the diamond represents the parameters of the benchmark in Zhang (2018) (point Z). Points B and C, on the same $E_{\rm max}$ contour as the best fit, are used as additional points for discussing the radiation density in the source (see the text and Figure 4).

injected $\mathcal{L}_{\rm inj} = 4.1 \times 10^{46}\ {\rm erg\ Mpc^{-3}\ yr^{-1}}$ (both quantities have been calculated above 10^{16} eV). The baryonic loading required at the best fit is $\xi_A \sim 10$, if we take into account the local rate of LL-GRBs obtained in Liang et al. (2007) and a burst duration of $2 \cdot 10^5$ s. Interestingly, this is consistent with pioneering predictions (Waxman & Bahcall 1997), and it is substantially smaller than what is found with source-propagation models taking into account HL-GRBs as UHECR and neutrino sources (Baerwald et al. 2015; Biehl et al. 2018a). Note, however, that it is degenerate with the local rate and duration of the GRBs, and it may be accordingly higher for shorter durations expected from observations.

In order to discuss what the effect of the radiation density in the source on the cosmic-ray and neutrino fluxes is, we show in Figure 4 the same observables as in the upper panel of Figure 3, for the three parameter sets marked in Figure 2. These parameter sets have been chosen to lie in the same maximum energy contour, so that the cosmic-ray spectra at Earth corresponding to each set exhibit similar cutoffs at the highest energies. Moving from point C to B, the enhanced radiation density in the source increases the efficiency of the interactions, producing a growing flux of light elements, which is preserved after propagation through the extragalactic space (see the red lines in the left panel of Figure 4). The neutrinos produced in the development of the cascade in the source, as shown in the right panel of Figure 4, are strictly related to the efficiency of the disintegration in the source. The use of the source-propagation model breaks the degeneracy of the interpretation of the CR data: while both model A and B reproduce the CR spectrum above the ankle, the corresponding neutrino fluxes are clearly separated, as model B is in the "empty cascade" region. This discrimination power is lost in the cosmogenic neutrino fluxes, due to the similar maximum energies of the parameter sets we used for this discussion.

The description of the cosmic-ray data across the ankle is a very controversial issue. Although the spectrum above EeV energies can be in principle reproduced with a one-source population (as done for example in Biehl et al. 2018a), the measured composition (Aab et al. 2014) cannot be described by models having a prevailing light component at low energies. On the other hand, the copious production of nucleons in the interactions in the source and in the extragalactic propagation naturally grants a lighter composition while decreasing the energy. We then argue that the presence of the cutoff of the Galactic cosmic-ray population could account for a certain percentage of the CR flux at ∼EeV, similar to what has been done already in, for example, Aloisio et al. (2014), Unger et al. (2015), Globus et al. (2015b), and Aab et al. (2017), and reconcile the expected composition with the measurements, as is shown in the upper left and lower panels of Figure 3. With the introduction of this sub-ankle component, the CR spectrum can be reproduced above the EeV energies and the composition becomes heavier than what it could be if only the protons produced in the propagation were considered below the ankle. Fixing the chemical composition of the sub-ankle contribution to $A = 28$, the spectral index of this component is found to be $\alpha_{\rm gal} = 4.2$ and the fraction of the corresponding flux at $\log_{10}(E/[{\rm eV}]) = 17.5$ is ∼78%. The slope of the sub-ankle flux and the percentage of that with respect to the extragalactic one at ∼EeV are also influenced by the source evolution, as already pointed out in Globus et al. (2015b). Having investigated the effect of m in the fit results, we choose here $m = 1$ (closer to the GRB redshift evolution indicated in Kistler et al. (2009) than the SFR, corresponding to $m = 0$ in our parameterization). Although the choice of the SFR evolution with respect to a

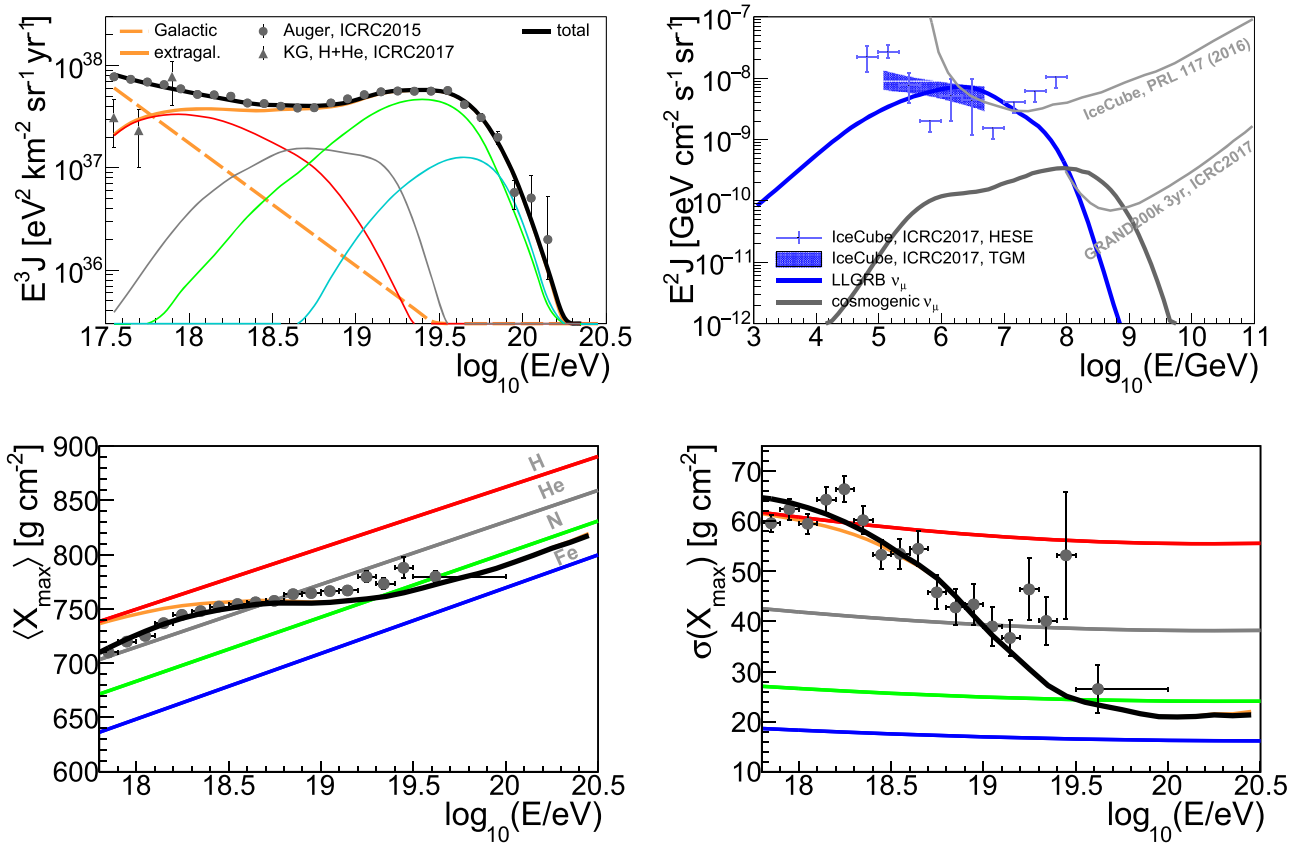

Figure 3. Cosmic-ray and neutrino observables corresponding to a parameter space point describing both UHECR and neutrino data at the highest energies (denoted by the stars in Figure 2, $L = 10^{46.8}$ erg s^{-1}, $R = 10^9$ km, with $\xi_A \approx 10$). Upper right panel: the predicted muon neutrino spectrum from LL-GRBs and cosmogenic neutrinos, compared respectively to the data from the High Energy Starting Events (HESE) and the Through Going Muons (TGM) at IceCube (Kopper 2017) and to the cosmogenic limits from IceCube (Aartsen et al. 2016) and GRAND (Fang et al. 2017). Upper left panel: simulated energy spectrum of UHECRs, multiplied by E^3; and its (extragalactic) components from (groups of) different nuclear species (thin, groups defined as in Figure 1). The orange dashed curve represents the sub-ankle component (which may be of Galactic origin), while the solid orange curve represents the extragalactic one. For comparison, the Auger data points from Valiño et al. (2015) and the KASCADE-Grande data points (for the light component, H and He) from Schoo et al. (2017) are shown. Lower panels: predictions (sub-ankle and extragalactic, thick black curve, and extragalactic-only, thin orange curve) and data (Porcelli et al. 2015) on the average (left) and standard deviation (right) of the $X_{\rm max}$ distributions as a function of the energy. For predictions, EPOS-LHC (Pierog et al. 2015) is assumed as the interaction model for UHECR-air interactions.

stronger one does not qualitatively affect the fit results, the nucleon flux at ∼EeV is lower if $m = 0$, requiring as a consequence a larger $f_{\rm Gal}$ to reproduce the sub-ankle spectrum. Another consequence is that the cosmogenic neutrino flux is expected to be lower by a factor ∼2 corresponding to the best fit presented here, if SFR is used. Conversely, $m > 1$ may be used to eliminate the Galactic contribution in the spectral fit; however, the flux will be still dominated by nucleons below the ankle, leading to a tension with the composition data in that case. It is also important to stress that the cosmological evolution of the LL-GRB population is yet unconstrained, due to limitations in observations. The source evolution used here is consistent with the diffusive gamma-ray background (see Globus et al. 2017).

It is also interesting to note that the cosmogenic neutrino flux is within the reach of the GRAND experiment (Fang et al. 2017). This is different from what has been found to correspond to the hypothesis that the common origin of UHECRs and neutrinos is tidal disruption events (TDEs; in Biehl et al. 2018b), which are expected to have a negative evolution with redshift. However, due to the low number of detections, the evolution of the LL-GRBs with redshift is uncertain. As already pointed out in, for example, Heinze et al. (2016), Aab et al. (2017), and Alves Batista et al. (2019), an anti-correlation between the spectral index of the ejected cosmic-ray flux and the value of m exists. This is due to the fact that a positive evolution with redshift naturally softens the propagated CR flux at the lowest energies, allowing very hard CR spectra to escape from the source; the escape mechanism used in this work corresponds to an effective spectrum $\propto E^3$. Vice versa, for a negative evolution, it is natural to expect softer CR spectra at the escape from the source, compared to what is used here ($\propto E^{-1}$, corresponding to the direct escape). While a consistent description of the UHECRs and PeV neutrino data points can be found in the two different scenarios of TDE and LL-GRB sources, what distinguishes these descriptions is the detectability of the cosmogenic neutrinos, which strongly depends on the redshift evolution.

Sources with dense radiation fields are usually opaque to high-energy gamma-rays, as they scatter off the lower energy X-ray photons in annihilation processes. However, the target photon spectrum is only measured in a small energy band and its behavior beyond that is uncertain. In Murase et al. (2016) and Biehl et al. (2018b), it has been shown that, depending on the spectral indices, the source can be optically thick to gamma-rays ranging from MeV to PeV. For the spectral indices we use in this work, gamma-rays even beyond PeV energies could be trapped. To get a rough estimate of the detection potential, we calculated the gamma-ray cascades from escaping EeV photons originating from π^0 decays. In fact, we find that

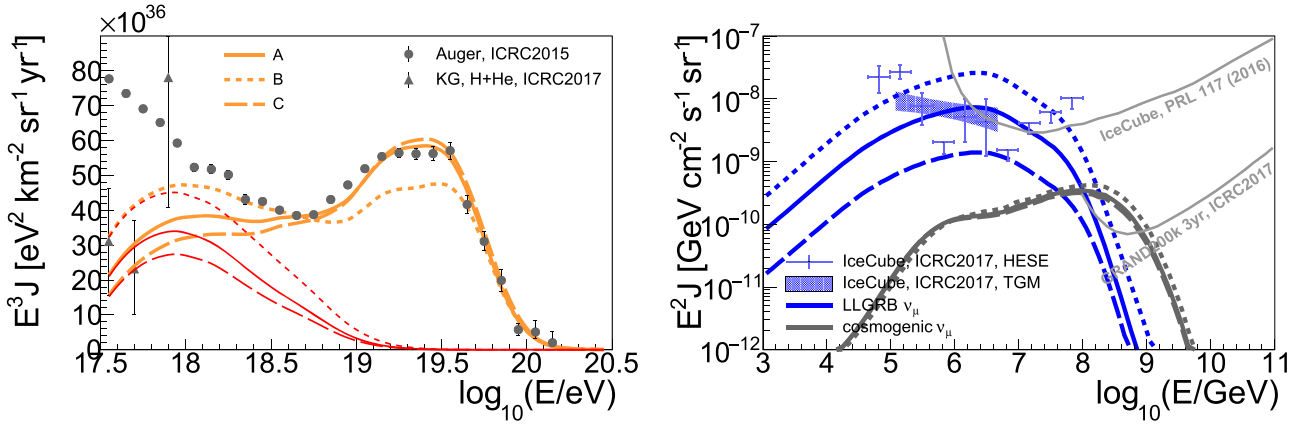

Figure 4. Cosmic-ray (left panel, multiplied by E^3, linear scale) and neutrino (right panel, multiplied by E^2) fluxes at Earth corresponding to a parameter space point describing both UHECR and neutrino data at the highest energies reported in Figure 2 (point A) and to cases with similar cutoff energies at the source, but different values for the luminosity and the radius (points B and C), i.e., different strengths of the nuclear cascade (see Figure 2, left panel). In the left panel, the all-particle flux (orange) is shown together with the nucleon contribution (red) of the cosmic-ray flux.

high-energy photons can be expected in an energy range from MeV to TeV, which is suitable for CTA, for example. Further investigation is needed to determine whether the expected sensitivity of CTA above 10 GeV (The Cherenkov Telescope Array Consortium et al. 2017) can be reached, as it depends very much on the low-energy target photons.

The systematic uncertainty on the measured CR scale has not been taken into account in this work, which means that our model can reproduce the UHECR data even at the energy calibration face value. Note, however, that the energy calibration is degenerate with the acceleration efficiency, which means that solid conclusions on the shift of the energy scale or the acceleration efficiency cannot be obtained (Biehl et al. 2018b). We have also tested a distribution of sources over luminosity, using the luminosity function as defined in Liang et al. (2007). Since the results are very similar to our Figure 3 for appropriate choices of collision radius and acceleration efficiency, we do not explicitly show them here.

4. Summary and Conclusions

We have demonstrated that a global description of the cosmic-ray and neutrino data at the highest energies can be obtained by considering LL-GRBs as sites of acceleration and interaction of cosmic rays. We have shown that if the diffuse neutrino flux is to be powered by LL-GRBs, high photon densities in the source are required for efficient neutrino production. As a consequence, nuclei will disintegrate in the source, and the nuclear cascade developing within the source has to be taken into account. Our results are therefore based on a source-propagation model including the nuclear cascade in the source and cosmic-ray propagation.

Interestingly, the light nuclei and nucleons (protons and neutrons) produced in the nuclear cascade can be used to describe the cosmic-ray spectrum and composition below the ankle at $5 \cdot 10^{18}$ eV. For a detailed analysis, we have included the next population dominating the cosmic-ray flux at energies $\lesssim 7 \cdot 10^{17}$ eV as an unconstrained additional model component—which may be of Galactic origin. As a consequence, we have obtained a near-perfect description of cosmic-ray spectrum and composition across the ankle, while at the same time powering the neutrino flux at the highest energies.

In conclusion, efficient modeling of the processes in the jet with extragalactic propagation allows a direct connection between the data and the characteristics of the source. The investigation of alternative source classes to HL-GRBs and AGN blazars is motivated by constraints on the diffuse contribution from recent IceCube stacking analyses. Therefore, alternative scenarios, including LL-GRBs, are potentially needed to describe the diffuse IceCube neutrinos. If the connection between neutrinos and UHECRs exists, it is likely that strong enough magnetic field effects on the secondary pions, muons, and kaons break the correlation between neutrino peak energy and maximal cosmic-ray energy, as we have seen in LL-GRBs. For the same reason, it is difficult to postulate the UHECR connection in AGN blazars (Murase et al. 2014; Gao et al. 2018; Rodrigues et al. 2018). Thanks to our estimate of the gamma-ray cascades from escaping EeV photons, we strongly encourage future experimental studies of candidate source classes such as LL-GRBs from CTA.

We thank A. Palladino, S. Petrera, I. Sadeh, and M. Unger for useful discussions. This work has been supported by the European Research Council (ERC) under the European Union's Horizon 2020 research and innovation programme (grant No. 646623).

Software: NeuCosmA (Biehl et al. 2018a, 2018b), SOPHIA (Mucke et al. 2000), SimProp (Aloisio et al. 2017), CRPropa 2 (Kampert et al. 2013), TALYS (Koning et al. 2007).

ORCID iDs

Walter Winter https://orcid.org/0000-0001-7062-0289

References

Aab, A., Abreu, P., Aglietta, M., et al. 2014, PhRvD, 90, 122005
Aab, A., Abreu, P., Aglietta, M., et al. 2017, JCAP, 1704, 038
Aartsen, M. G., Abraham, K., Ackermann, M., et al. 2016, PhRvL, 117, 241101
Aartsen, M. G., Ackermann, M., Adams, J., et al. 2017, ApJ, 843, 112
Abbasi, R., Ahlers, M., Andeen, K., et al. 2012, Natur, 484, 351
Aloisio, R., Berezinsky, V., & Blasi, P. 2014, JCAP, 1410, 020
Aloisio, R., Boncioli, D., Di Matteo, A., et al. 2017, JCAP, 1711, 009
Aloy, M.-n., Cuesta-Martínez, C. F., & Obergaulinger, M. 2018, MNRAS, 478, 3576
Alves Batista, R., Boncioli, D., di Matteo, A., van Vliet, A., & Walz, D. 2015, JCAP, 1510, 063

Alves Batista, R., de Almeida, R. M., Lago, B., & Kotera, K. 2019, JCAP, 2019, 002
Baerwald, P., Bustamante, M., & Winter, W. 2013, ApJ, 768, 186
Baerwald, P., Bustamante, M., & Winter, W. 2015, APh, 62, 66
Biehl, D., Boncioli, D., Fedynitch, A., & Winter, W. 2018a, A&A, 611, A101
Biehl, D., Boncioli, D., Lunardini, C., & Winter, W. 2018b, NatSR, 8, 10828
Boncioli, D., Fedynitch, A., & Winter, W. 2017, NatSR, 7, 4882
Bromberg, O., Nakar, E., & Piran, T. 2011, ApJL, 739, L55
Bustamante, M., Baerwald, P., Murase, K., & Winter, W. 2015, NatCo, 6, 6783
Bustamante, M., Murase, K., Winter, W., & Heinze, J. 2017, ApJ, 837, 33
Fang, K., Álvarez-Muñiz, J., Alves Batista, R., et al. 2017, PoS, 996, ICRC2017
Fenu, F., Aab, A., Abreu, P., et al. 2017, PoS, 486 ICRC2017
Gao, S., Fedynitch, A., Winter, W., & Pohl, M. 2018, arXiv:1807.04275
Gilmore, R. C., Somerville, R. S., Primack, J. R., & Dominguez, A. 2012, MNRAS, 422, 3189
Globus, N., Allard, D., Mochkovitch, R., & Parizot, E. 2015a, MNRAS, 451, 751
Globus, N., Allard, D., & Parizot, E. 2015b, PhRvD, 92, 021302
Globus, N., Allard, D., Parizot, E., & Piran, T. 2017, ApJL, 839, L22
Guetta, D., & Della Valle, M. 2007, ApJL, 657, L73
He, H.-N., Kusenko, A., Nagataki, S., Fan, Y.-Z., & Wei, D.-M. 2018, ApJ, 856, 119
Heinze, J., Boncioli, D., Bustamante, M., & Winter, W. 2016, ApJ, 825, 122
Hopkins, A. M., & Beacom, J. F. 2006, ApJ, 651, 142
Kampert, K.-H., Kulbartz, J., Maccione, L., et al. 2013, APh, 42, 41
Kistler, M. D., Yüksel, H., Beacom, J. F., Hopkins, A. M., & Wyithe, J. S. B. 2009, ApJL, 705, L104
Koning, A. J., Hilaire, S., & Duijvestijn, M. C. 2007, in Proc. Int. Conf. Nuclear Data for Science and Tecnology (Les Ulis: EDP Sciences), 211
Kopper, C. 2017, PoS, 981 ICRC2017
Liang, E., Zhang, B., & Dai, Z. G. 2007, ApJ, 662, 1111
Liu, R.-Y., Wang, X.-Y., & Dai, Z.-G. 2011, MNRAS, 418, 1382
Mucke, A., Engel, R., Rachen, J., Protheroe, R., & Stanev, T. 2000, CoPhC, 124, 290
Murase, K., Guetta, D., & Ahlers, M. 2016, PhRvL, 116, 071101
Murase, K., Inoue, Y., & Dermer, C. D. 2014, PhRvD, 90, 023007
Murase, K., & Ioka, K. 2013, PhRvL, 111, 121102
Murase, K., Ioka, K., Nagataki, S., & Nakamura, T. 2006, ApJL, 651, L5
Murase, K., Ioka, K., Nagataki, S., & Nakamura, T. 2008, PhRvD, 78, 023005
Ohira, Y., Murase, K., & Yamazaki, R. 2010, A&A, 513, A17
Palladino, A., & Winter, W. 2018, A&A, 615, A168
Pierog, T., Karpenko, I., Katzy, J. M., Yatsenko, E., & Werner, K. 2015, PhRvC, 92, 034906
Pierre Auger Collaboration 2013, JCAP, 2013, 026
Piran, T. 2004, RvMP, 76, 1143
Porcelli, A., Aab, A., Abreu, P., et al. 2015, PoS, 420 ICRC2015
Rodrigues, X., Fedynitch, A., Gao, S., Boncioli, D., & Winter, W. 2018, ApJ, 854, 54
Schoo, S., Kang, D., Apel, W. D., et al. 2017, PoS, 339 ICRC2017
Senno, N., Murase, K., & Meszaros, P. 2016, PhRvD, 93, 083003
Sun, H., Zhang, B., & Li, Z. 2015, ApJ, 812, 33
The Cherenkov Telescope Array Consortium, Acharya, B. S., Agudo, I., et al. 2017, arXiv:1709.07997
Unger, M., Farrar, G. R., & Anchordoqui, L. A. 2015, PhRvD, 92, 123001
Valiño, I., Aab, A., Abreu, P., et al. 2015, PoS, 271 ICRC2015
Virgili, F., Liang, E., & Zhang, B. 2009, MNRAS, 392, 91
Waxman, E., & Bahcall, J. N. 1997, PhRvL, 78, 2292
Woosley, S., & Heger, A. 2006, ApJ, 637, 914
Zhang, B. T., Murase, K., Kimura, S. S., Horiuchi, S., & Mészáros, P. 2018, PhRvD, 97, 083010